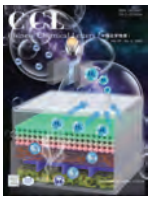
Chinese Chemical Letters 37 (2026) 111901

Contents lists available at ScienceDirect

Chinese Chemical Letters

journal homepage: www.elsevier.com/locate/cclet



Self-assembled cyclodextrin-porphyrin nanoplatform for synergistic chemo-phototherapy and targeted delivery of camptothecin against breast cancer

Jiaojiao Yang[a,b,1], Shaokun Yang[a,b,1], Wei Cheng[c], Jie Wu[c], Haijing Qu[c], Han Chen[c], Zhiran Duan[c], Yuqing Pan[c], Ning Wang[c], Chao Wang[c], Jian Gao[a], Bai Xiang[a,b,*], Xiangdong Xue[c,*]

[a] *Hebei Key Laboratory of Innovative Drug Research and Evaluation, School of Pharmaceutical Sciences, Hebei Medical University, Shijiazhuang 050017, China*
[b] *National Key Laboratory of New Pharmaceutical Preparations and Excipients, Shijiazhuang 050017, China*
[c] *Shanghai Frontiers Science Center of Drug Target Identification and Delivery, School of Pharmaceutical Sciences, National Key Laboratory of Innovative Immunotherapy, Shanghai Jiao Tong University, Shanghai 200240, China*

ARTICLE INFO

Article history:
Received 3 July 2025
Revised 23 September 2025
Accepted 25 September 2025
Available online 25 September 2025

Keywords:
Breast cancer
Drug delivery
Camptothecin
PDT
PTT

ABSTRACT

The management of breast cancer remains clinically intractable, driven by its highly invasive behavior and limited susceptibility to conventional treatments. In this study, we engineered an innovative cyclodextrin-porphyrin co-assembled nanoplatform (CT NPs) to enable multimodal breast cancer therapy. By successfully encapsulating camptothecin (CPT) within this nanocarrier, the system (CTC NPs) achieved synergistic chemo-phototherapeutic efficacy through dual-modality action. The highly biocompatible cyclodextrin carrier significantly improved the physicochemical characteristics of CPT. *In vivo* studies revealed that CTC NPs effectively evaded clearance by the reticuloendothelial system, overcame the defect of premature drug leakage, and exhibited superior tumor targeting and infiltration capabilities. Under near-infrared (NIR) laser irradiation, CTC NPs can simultaneously induce localized hyperthermia and produce reactive oxygen species (ROS), thereby achieving efficient tumor ablation. In 4T1 tumor-bearing mice, CTC NPs exhibited targeted, safe, and highly potent anti-tumor efficacy, significantly suppressing both primary tumor progression (tumor suppression rate $> 95\%$) and metastatic dissemination. In summary, this integrated nanoplatform establishes a novel theranostic paradigm for synergistic chemo-phototherapy against triple-negative breast cancer (TNBC), achieving precise tumor ablation through NIR-triggered drug release and real-time imaging guidance.

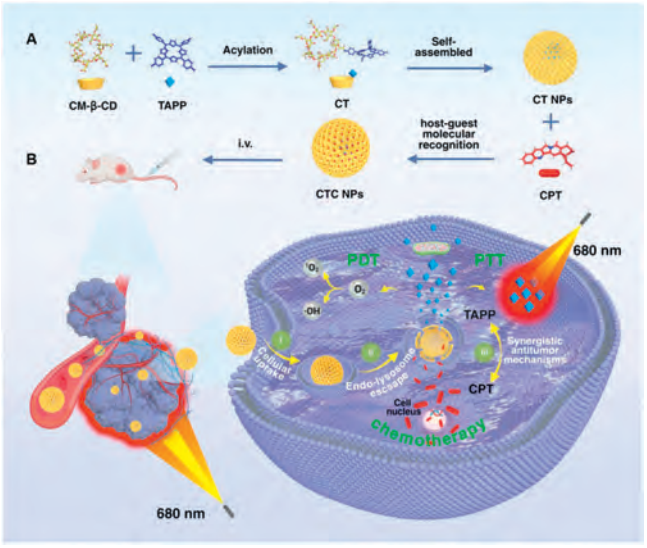
© 2026 Published by Elsevier B.V. on behalf of Chinese Chemical Society and Institute of Materia Medica, Chinese Academy of Medical Sciences.

Breast cancer remains a major global health burden, ranking among the most prevalent malignant neoplasms affecting women worldwide. Current estimates project that by 2040, breast cancer incidence will exceed three million new annual cases and cause one million deaths [1–3]. Its highly invasive nature and pronounced metastatic potential pose significant challenges to achieving curative outcomes [4,5]. While surgical lesion excision faces inherent limitations, combination chemotherapy represents the primary clinical strategy [6–8]. Camptothecin (CPT), a natural anticancer agent derived from *Camptotheca acuminata*, demonstrates high efficacy against diverse cancers [9–14]. However, its clinical utility is hindered by suboptimal physicochemical properties and delivery challenges [15–17], prompting exploration of nanomedicine-based CPT delivery systems [18–22].

Cyclodextrins (CDs), cyclic oligosaccharides featuring hydrophilic exteriors and hydrophobic cavities [23,24], are ideal drug carriers due to their exceptional biocompatibility, low immunogenicity, minimal toxicity, and high bioavailability [25–27]. Their hydrophobic cavities efficiently encapsulate lipophilic compounds, including hydrophobic therapeutics [28]. Carboxymethyl-β-cyclodextrin (CM-β-CD) exhibits superior host-guest binding affinity, favorable biocompatibility with anticancer agents, and an enhanced safety profile, making it a promising carrier for structurally diverse pharmaceuticals [29–32].

* Corresponding authors.
E-mail addresses: baixiang@hebmu.edu.cn (B. Xiang), xuexd@sjtu.edu.cn (X. Xue).
[1] These authors contributed equally to this work.

https://doi.org/10.1016/j.cclet.2025.111901
1001-8417/© 2026 Published by Elsevier B.V. on behalf of Chinese Chemical Society and Institute of Materia Medica, Chinese Academy of Medical Sciences.



Scheme 1. Construction of cyclodextrin-based self-assembled nanoparticles CTC NPs (A) and their anti-tumor mechanism (B).

Photodynamic therapy (PDT) and photothermal therapy (PTT) have recently gained significant attention for their high therapeutic efficacy, tumor-specific ablation, minimal side effects, and low risk of inducing drug resistance [33–39]. Photosensitizers activated by light generate reactive oxygen species (ROS) from molecular oxygen to mediate tumor cell death, while localized photothermal effects synergistically enhance treatment outcomes [40–43]. Porphyrin-based compounds, with their rigid conjugated frameworks and broad-spectrum photon absorption, serve as canonical photosensitizers [44]. Among these, 5,10,15,20-tetrakis(4-aminophenyl)porphyrin (TAPP) demonstrates exceptional chemical stability, high photothermal conversion efficiency, and potent photodynamic activity, establishing it as a high-performance dual-modal photosensitizer [45–47].

In this study, we developed a novel cyclodextrin-porphyrin nanoplatform *via* dynamic self-assembly for tumor-targeted delivery of CPT and integrated breast cancer theranostics (Scheme 1). Initially, CM-β-CD was conjugated with TAPP to form a functionalized host complex (TAPP-CM-β-CD), which underwent hydrogen-bond-driven self-assembly into TAPP-CM-β-CD nanoparticles (CT NPs) in aqueous media. Subsequent host-guest interactions enabled the precise encapsulation of CPT within the hydrophobic cavity of CM-β-CD, yielding drug-loaded CPT@TAPP-CM-β-CD nanoparticles (CTC NPs). Critically, TAPP integration conferred dual photodynamic and photothermal functionality, providing exceptional ROS generation, high photothermal conversion efficiency ($\eta = 43.9\,\%$), and enhanced photostability while enabling CPT/TAPP-mediated multimodal therapy. The nanoplatform demonstrated optimized biodistribution and pharmacokinetics, effective evasion of the reticuloendothelial system (RES), and significantly enhanced tumor accumulation ($\geq$2-fold) with deep tissue penetration. Furthermore, TAPP potentiated amplified photothermal responsiveness. The active targeting and intrinsic fluorescence of CTC NPs permitted precise tumor-normal tissue discrimination during *in vivo* imaging, underscoring their translational potential as a breast cancer nanotheranostic platform.

It has been demonstrated that CPT is capable of being encapsulated within the hydrophobic inner cavity of β-CD [48]. Therefore, CM-β-CD, a derivative of β-CD, demonstrates considerable potential for encapsulating CPT. To investigate the spatial configuration between CM-β-CD and CPT and to verify whether CM-β-CD is able to undergo host-guest complexation with CPT, relevant kinetic simulations were performed. The root mean square deviation (RMSD), solvent accessible surface area (SASA), and different moments control plots of molecular dynamics simulation trajectories in the system (Fig. 1A, Figs. S1 and S2 in Supporting information) revealed that the subject molecule and the guest molecule were rapidly combined to reach the optimal binding conformation at the initial moment, and the whole system was very stable. The CPT was tightly bound to the CM-β-CD, and the average free energy of binding was -36.75 kcal/mol (Figs. S3, S4 and Table S1 in Supporting information). It is well established that carboxyl (-COOH) and amino (-NH_2) groups are capable of undergoing condensation *via* amidation [49,50]. Consequently, the activated carboxyl group of CM-β-CD can condense with the amino group of TAPP to form a new cyclodextrin derivative, TAPP-CM-β-CD, which exhibits photosensitizing properties. TAPP-CM-β-CD self-assembled into spherical nanostructures *via* hydrogen bonding in water. CPT was then encapsulated within the hydrophobic cavity of the TAPP-CM-β-CD by means of host-guest complexation, forming the CPT@TAPP-CM-β-CD (CTC NPs). Applying heating and stirring techniques enhanced non-covalent interaction formation, facilitated the dynamic self-assembly process of non-covalent molecular recognition and accelerated inclusion complex formation [51].

The hydrodynamic diameters of CTC NPs and CT NPs were 100.96 ± 6.34 and 89.58 ± 7.31 nm by dynamic light scattering (DLS), respectively (Fig. 1B). After loading CPT, the surface charge of the NPs changed from -23.5 mV to -19.6 mV (Fig. 1C). Transmission electron microscopy (TEM) images (Fig. 1D) showed that the CTC NPs were uniformly dispersed, regular spherical particles with an average diameter of about 80 nm. This result was in agreement with the DLS measurements. The ultraviolet-visible (UV–vis) spectrum of the CTC NPs showed a characteristic absorption peak at 450 nm, which was red-shifted by 20 nm compared with the free TAPP (Fig. 1E). In addition, no additional absorption peak was observed for CPT (366 nm). Meanwhile, CTC NPs showed fluorescence quenching at 680 nm (Fig. 1F). These observations were attributed to the different states of the molecules (free/encapsulated/coupled), thus confirming the successful self-assembly of CTC NPs.

In the simulated blood environment, the two nanoparticles (CT NPs and CTC NPs) showed excellent stability with minimal changes in particle size and polydispersity index (PDI) (Fig. 1G and Fig. S5 in Supporting information). Quantification of CPT encapsulated in CTC NPs showed that the encapsulation and loading efficiencies of CPT were 87.2 % and 9.9 %, respectively (Fig. S6 in Supporting information). It is noteworthy that, under simulated blood circulation conditions (*i.e.*, without the addition of surfactants), the rate of drug leakage from the CTC NPs remained below 5 % within 24 h, thereby demonstrating excellent nanostructural integrity. However, when sodium dodecyl sulphate (SDS) was used to disrupt the nanostructure, the drug release rate rapidly increased to 60 % (Fig. 1H). This phenomenon confirms that the nanoplatform possesses a unique 'stable-responsive' dual characteristic: it maintains high stability during *in vivo* circulation, and after being enriched at the tumor site through enhanced permeability and retention (EPR) effects, its nanostructure can be specifically disrupted by the tumor microenvironment, thereby achieving targeted drug release and efficient accumulation. It is imperative to consider that, following the accumulation of CTC NPs at the tumor site, laser irradiation instigates a dual activation mechanism. Firstly, the laser activates the TAPP, resulting in the generation of ROS and local high temperatures. This process achieves synergistic effects of PDT and PTT. Secondly, laser stimulation and photothermal effects significantly promote the burst release of CPT, rapidly increasing the local drug concentration in the tumor to the therapeutic threshold (Fig. 1I). This spatiotemporal dual-regulation activation mode ensures the safety of NPs in normal tissues and significantly enhances antitu-

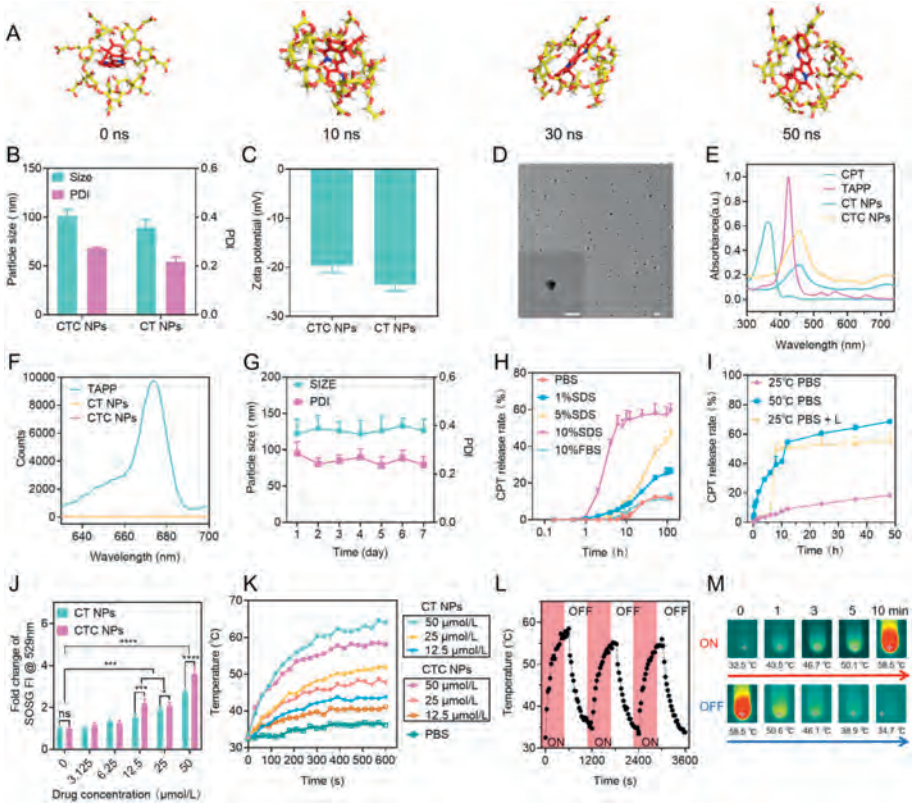


Fig. 1. Characterization of CTC NPs. (A) Comparison of the complex conformation at different moments of the CM-β-CD-CPT system. Size distribution, PDI (B) and zeta potential (C) of CTC NPs and CT NPs. (D) TEM image of CTC NPs. Scale bar: 100 nm (left), 200 nm (right). (E) UV–vis scan patterns of free CPT, free TAPP, CT NPs and CTC NPs (5 μmol/L). (F) Fluorescence spectra of free TAPP, CT NPs and CTC NPs (5 μmol/L) with excitation wavelength 430 nm. (G) 7-day stability of CTC NPs in PBS containing 10 % FBS. (H) Percentage of cumulative drug release from CTC NPs (1 mmol/L) in different environments. (I) Percentage of cumulative drug release from CTC NPs under 680 nm laser stimulation and at 50 °C. (J) Indications of ROS production by CTC NPs and photodynamic effects of CT NPs using SOSG as an indicator. (K) Photothermal effects of CTC NPs and CT NPs under 680 nm laser irradiation: photothermal heating curves (L) and thermal images (M) of CTC NPs during three 'ON/OFF' laser irradiation cycles. Data are expressed as means ± standard deviation (SD) ($n = 3$). $^{***}P < 0.001$, $^{****}P < 0.0001$. ns: no significance.

mor activity through multiple synergistic effects. The experimental data demonstrate that this smart, responsive drug delivery system achieves precise spatiotemporal control of drug release, thus providing a new strategy for combined tumor therapy. CTC NPs have been engineered to trigger the release of the drug in real time using a near-infrared laser (680 nm), thereby enabling precise control of on-demand drug delivery to the lesion site and avoiding toxicity caused by systemic exposure.

In tumor phototherapy, the photodynamic properties and photothermal conversion rate of photosensitizers are key factors affecting efficacy. We used the singlet oxygen sensor green (SOSG) probe to assess the ability of CTC NPs to generate ROS under laser irradiation. The photodynamic properties of both NPs were concentration-dependent (Fig. 1J). The fluorescence signals of CT NPs and CTC NPs were significantly enhanced after irradiation (680 nm, 0.4 W/cm^2, 5 min), with a 2.8- and 3.6-fold increase, respectively, compared with the control group. These results confirm that TAPP can effectively endow the carriers with strong photodynamic ability. Subsequently, the photothermal conversion ability of CTC NPs was evaluated. Fig. 1K shows the heating curves of CT NPs and CTC NPs at different concentrations under 680 nm laser (0.4 W/cm^2) irradiation. The photothermal conversion effect of the two NPs is very pronounced and exhibits a dual dependence on concentration and irradiation time. Under laser irradiation, the temperature of both NPs solutions increased significantly, reaching over 50 °C in a short time. This temperature is sufficient to kill the tumor cells, which meets the requirement of tumor thermotherapy. The photothermal conversion efficiency (η) was 43.9 %, and the system time constant (τ) was 267.8 s (Fig. S7 in Supporting information). The photostability was also evaluated by the temperature change of the solution during light irradiation and subsequent cooling (Figs. 1L and M). After several cycles, the CTC NPs exhibited excellent photostability and thermal stability. These findings suggest that TAPP-mediated conversion of CTC NPs into effective photosensitizers has potential for application in PTT/PDT.

The cellular uptake and subcellular distribution of CPT-containing materials (CPT, CTC NPs) were investigated through the intrinsic fluorescence of CPT (366 nm). Initially, the intrinsic fluorescence (366 nm) of CPT was quantified by flow cytometry following the incubation of 4T1 cells with CPT or CTC NPs for varying periods (Fig. 2A and Fig. S8 in Supporting information). CTC NPs were internalised by 4T1 cells *via* the endocytosis pathway (Fig. S9 in Supporting information), and this process exhibited significant time-dependent characteristics. The CTC NPs group exhibited a stronger fluorescence signal compared to free CPT, indicating a greater efficiency of cellular internalization. This is attributable to the suboptimal physicochemical properties of CPT, which render it challenging to be ingested by cells. In contrast, CTC NPs are more prone to enter cells *via* endocytosis. This suggests that the nanoplatform enhances cellular uptake and elevates intracellular drug concentration, thereby augmenting its antitumor efficacy. Subsequently, the intracellular distribution of CTC NPs was visualized by confocal laser scanning microscopy (CLSM) (Fig. 2B and Fig. S10 in Supporting information). Once internalized by 4T1 cells, CTC NPs could be precisely localized within lysosomes. The co-localization coefficients of CTC NPs and lysosomes at 4 and 12 h were 0.68 and 0.83, respectively, indicating that CTC NPs exhibited an effective lysosomal co-localization performance. In conclusion,

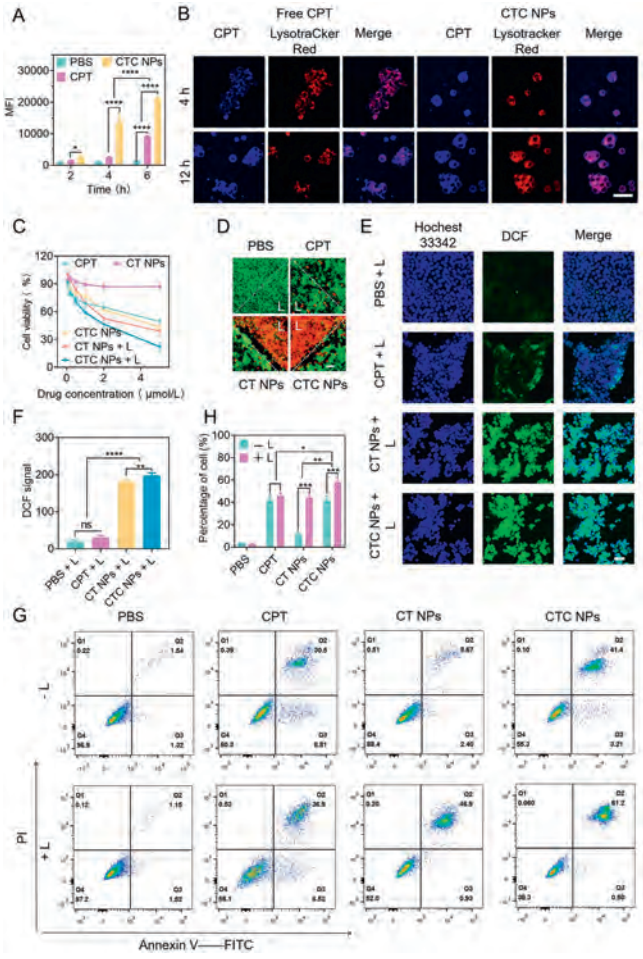


Fig. 2. *In vitro* antitumor effects of CTC NPs. (A) Cellular uptake of 4T1 cells after co-incubation with free CPT and CTC NPs for 2, 4 and 6 h. (B) Subcellular distribution of 4T1 cells after co-incubation with free CPT and CTC NPs for 4 and 12 h. Scale bar: 50 μm. (C) Viability of 4T1 cells treated with different materials. (D) Fluorescence images of calcein AM/PI stained 4T1 cells with or without 680 nm laser irradiation after different treatments. Scale bar: 100 μm. Production of ROS within cells under 680 nm laser irradiation (E) and quantitative analysis (F) in different treatment groups (5 μmol/L). Scale bar: 100 μm. Apoptosis (G) and quantitative analysis (H) of 4T1 cells after different treatments. Data are expressed as means ± SD ($n = 3$). $^{*}P < 0.05$, $^{**}P < 0.01$, $^{****}P < 0.0001$.

the high cellular uptake of CTC NPs can be attributed to two factors. Firstly, CTC NPs efficiently enter tumor cells through endocytosis, increasing intracellular drug accumulation. Alternatively, it can be attributed to the specific localization and retention properties of CTC NPs in lysosomes following their internalization into tumor cells.

The cytotoxicity of the various formulations was assessed using the methylthiazolyldiphenyl-tetrazolium bromide (MTT) assay (Fig. 2C). The CT NPs nanoplatform showed good biocompatibility. Cytotoxicity was significantly enhanced concentration-dependently for all material groups except CT NPs. Exposure of CT NPs and CTC NPs to laser light resulted in a significant decrease in cellular activity. The combined antitumor effect showed that the combined chemotherapeutic effect of CPT and the phototherapeutic effect of TAPP were significantly better than either drug alone (Fig. S11 in Supporting information).

The cytophototoxicity of both NPs was examined by observing live/dead cells after different treatments with calcein AM/PI cell viability and cytotoxicity assay kit (Fig. 2D). Laser irradiation elicited no significant effects on the PBS and CPT groups, indicating the absence of inherent laser cytotoxicity. In contrast, irradiation induced a significant phototoxic effect in cells treated with TAPP material. Notably, the number of live cells was significantly higher than the number of dead cells in the area that did not receive laser irradiation. Together, these findings suggest that CTC NPs are not only powerful phototherapeutic agents but also capable of eliminating tumor cells with a high degree of precision, making them promising for use in tumor therapy. The satisfactory phototoxicity prompted us to further investigate the photodynamic effects (Figs. 2E and F, Fig. S12 in Supporting information). The changes in the PBS and CPT groups were almost negligible, while both groups of CT NPs and CTC NPs showed significant green fluorescence from 2′,7′-dichlorofluorescein (DCF). In a word, the CTC NPs developed in this study retained the excellent photodynamic and photothermal properties of TAPP, and 5 min of laser irradiation produced sufficient intracellular heat and ROS generation for a potent antitumor effect. The introduced laser precisely kills tumors and avoids damaging cells in normal areas.

The investigation of cell death mechanisms was performed using the Annexin V-FITC Apoptosis Detection Kit. Apoptosis and necrosis are the two most prominent manifestations of cytotoxicity. Apoptosis of 4T1 cells with or without laser irradiation (680 nm, 0.4 W/cm^2, 5 min) was analyzed by flow cytometry after incubation with different materials for 24 h (Figs. 2G and H). Without combined laser treatment, apoptosis was not evident in the control and porphyrin carrier groups, and most cells grew normally. This is consistent with the results of the cytotoxicity experiments, further demonstrating the non-toxic and safe properties of the porphyrin carriers. The CPT-containing material group (CPT, CTC NPs) showed stronger apoptosis, proving that the apoptosis was mainly induced by the chemotherapeutic effect of CPT in the absence of laser presence. The CTC NPs group had higher intracellular drug accumulation and showed higher apoptosis (41.1 %) due to stronger internalization than free CPT. After the introduction of laser treatment (680 nm, 0.4 W/cm^2, 5 min), the apoptotic phenomenon in the control group remained negligible, and the apoptotic rate in the free CPT group was not significantly changed. This proved that the laser itself could not induce apoptosis production, and even laser irradiation did not damage normal cells. In the porphyrin-carrier group, the apoptosis rate significantly increased from 8.67 % to 46.9 % following irradiation, attributed to the apoptosis-inducing effects of the photodynamic and photothermal properties of the TAPP-loaded NPs. Combined with phototherapy, the CTC NPs further enhanced apoptosis, reaching 61.2 %. These results suggest that chemotherapy in combination with phototherapy can enhance the anti-tumor effect, and our designed nanoplatform in combination with PDT/PTT induced apoptosis in tumor cells with great potential for the treatment of malignant tumors, in line with our hypothesis.

The kinetic behavior *in vivo* was followed in real time using the fluorescent properties of TAPP (Figs. 3A and B). All animal experiments were conducted following the National Research Council's Guide for the Care and Use of Laboratory Animals and approved by the Experimental Animal Ethics Committee of the Laboratory Animal Centre of Shanghai Jiao Tong University (approval No. A2023232–002). After intravenous administration, the accumulation of free TAPP at the tumor site was low and cleared rapidly. The fluorescence of CTC NPs accumulated gradually at the tumor site, reaching the highest intensity at 6 h after administration. CTC NPs were more likely to accumulate at the tumor site and were almost completely cleared after 24 h of circulation in the body, and did not accumulate for a long time in the body to cause toxicity.

Six hours after the injection, heart, liver, spleen, lung, kidney, and tumor tissues from the mice were collected for *ex vivo* imaging (Figs. 3C and D). As a small molecule fluorophore, free TAPP lacks tumor-targeting ability and is preferentially cleared from liver and kidney tissues rather than accumulating at the tumor site.

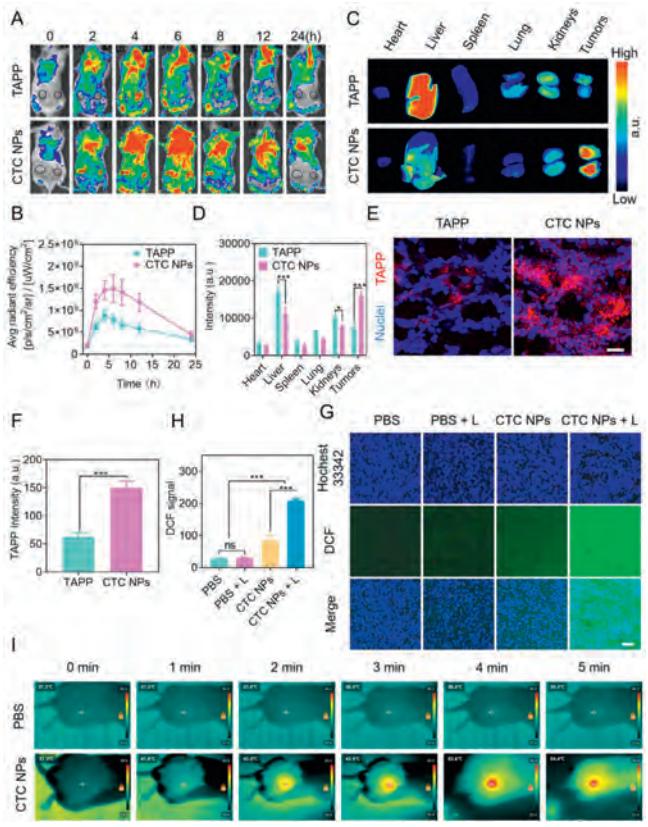


Fig. 3. *In vivo* performance of CTC NPs. Time-dependent tumor accumulation of free TAPP and CTC NPs (A) and quantitative fluorescence analysis (B). Major organ and tumor *ex vivo* imaging (C) and quantitative fluorescence analysis (D) after intravenous injection 6 h of free TAPP and CTC NPs. Frozen sections showing tumor accumulation (E) and quantitative analysis (F) of free TAPP and CTC NPs after intravenous injection 6 h, tumor nuclei were labelled with Hoechst 33,342. Scale bar: 50 μm. ROS generating capacity (G), quantitative analysis of ROS (H), and temperature change (I) of the tumor site under 680 nm laser irradiation, after intravenous injection 6 h of CTC NPs. Scale bar: 100 μm. Data are expressed as means ± SD ($n = 3$). $^{***}P < 0.001$.

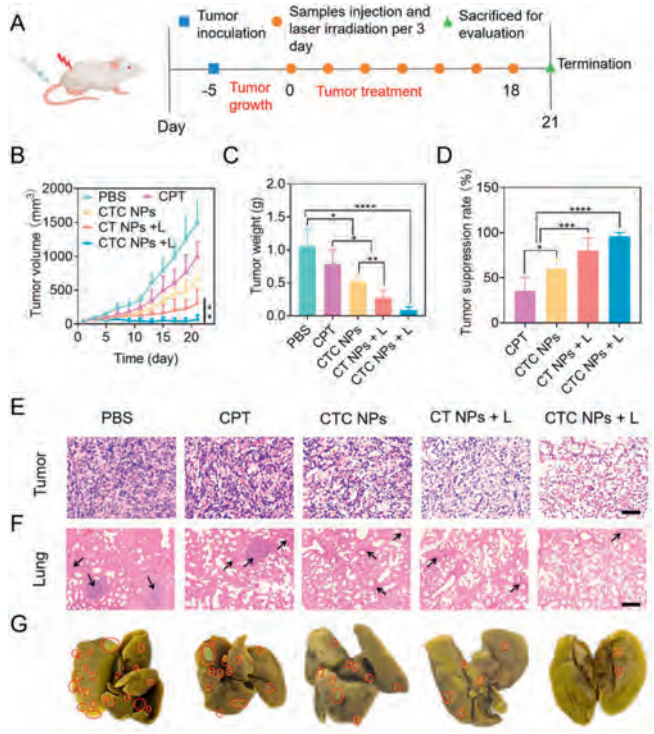


Fig. 4. *In vivo* anti-tumor efficacy of CTC NPs. (A) Tumor treatment protocol in 4T1 tumor-bearing mice. Tumor growth (B) in each group of mice during treatment ($n = 6$). Tumor weight (C), tumor inhibition rate (D) and H&E staining of isolated tumors (E) at the end of the treatment. Scale bar: 50 μm. Representative photographs of H&E staining (F) and Bouin's fixation (G) of metastatic lung tissue. Scale bar: 200 μm. Data are expressed as means ± SD. $^{*}P < 0.05$, $^{**}P < 0.01$, $^{***}P < 0.001$, $^{****}P < 0.0001$.

Compared with free TAPP, the distribution of CTC NPs in the liver, kidney, and spleen was significantly reduced, suggesting that the nanoplatform have RES scavenging ability, which may reduce the systemic toxicity of the drug *in vivo*. The fluorescence of TAPP and CTC NPs at the tumor site was observed (Figs. 3E and F). The CTC NPs effectively aggregated and infiltrated at the tumor site under the EPR effect. According to the quantitative results (Figs. 3B, D, and F), the accumulation of CTC NPs at the tumor site was about twice as much as that of free TAPP at 6 h after administration. The results confirmed the superior *in vivo* tumor-targeting ability of CTC NPs, which prolongs the *in vivo* circulation time of the drug and avoids the fate of the drug being rapidly cleared *in vivo*.

To validate the mechanism of CTC NPs mediated phototherapy in 4T1 tumor-bearing mice, further investigation was conducted into the tumor-site ROS production (Figs. 3G and H) and photothermal conversion ability (Fig. 3I) of CTC NPs. As anticipated, the tumor tissue exhibited minimal fluorescence even in the absence of external factors, reflecting the elevated ROS environment characteristic of the tumor. Irradiation with a laser did not result in a change to this situation. The application of a 680 nm laser (0.4 W/cm^2, 5 min) to tumor tissue infiltrated with CTC NPs resulted in TAPP-mediated ROS production, thereby enhancing the efficacy of cancer treatment. The temperature changes in tumors exposed to laser light were recorded using infrared thermography (Fig. 3I). No significant change in temperature was observed in the tumor site of the PBS group during light exposure. In contrast, the intratumor temperature of the CTC NPs-treated group increased gradually and reached a maximum of 54.4 °C after 5 min of laser exposure, which was significantly higher than that observed in the PBS group. The excellent photothermal conversion ability observed can be attributed to the high targeted delivery efficiency of CTC NPs and effective infiltration in the tumor site. The above results confirm that the excellent photodynamic properties and photothermal conversion ability of CTC NPs are sufficient to support the phototherapeutic function of the nanoformulation.

Based on the drug delivery efficiency and synergistic PDT/PTT antitumor effects of CTC NPs, we investigated the antitumor efficacy of CTC NPs in 4T1 tumor-bearing mice (Fig. 4A). Antitumor efficacy of each group was evaluated based on tumor growth curves (Fig. 4B and Fig. S13 in Supporting information), tumor photos (Fig. S14 in Supporting information), tumor weight (Fig. 4C) and tumor inhibition rate (Fig. 4D). PBS, as a negative control group, showed rapid tumor growth and little antitumor efficacy. The antitumor efficacy of the free CPT group was only slightly higher than that of the PBS group due to the low dose of CPT administered (relatively lower than those reported in the literature [23,52,53]) and low drug accumulation. In contrast, the nanoplatform improved drug targeting and tumor infiltration, a notably greater tumor inhibition rate was observed in the CTC NPs group when compared to the CPT group. Tumor growth was strongly inhibited by nano-porphyrin alone, which showed superior anti-tumor efficacy of PDT/PTT under laser irradiation (680 nm, 0.4 W/cm^2, 5 min). The combination of phototherapy and chemotherapy enhanced the therapeutic effect, and the tumor inhibition rate in the CTC NPs+ laser group was as high as 95.74 % ± 3.04 %, and the tumor was almost completely ablated under laser (680 nm, 0.4 W/cm^2, 5 min)

irradiation, which was higher than that in the CT NPs + laser group (80.42 % ± 15.32 %). In addition, the density and morphology of tumor cells in hematoxylin and eosin (H&E) paraffin sections were further observed (Fig. 4E). Compared to the other groups, the combined treatment of CTC NPs and laser resulted in the lowest tumor density and the highest tumor necrosis. These results suggest that CTC NPs can be considered an ideal platform for the treatment of 4T1 tumor-bearing mice models. The self-assembly of nanostructures offers systemic stability and benefits in targeted tumor drug delivery. Furthermore, multimodal therapy has been shown to result in tumor near eradication at the end of treatment.

The anti-tumor metastatic effect of the combination therapy was assessed using pulmonary metastatic nodules of 4T1 tumors (Figs. 4F and G). A substantial number of overt metastatic foci were evident in the lungs of mice in the control and CPT groups, exhibiting severe tumor infiltration, minimal presence of normal alveolar tissue, and extensive areas of tumor cells within the sectioned field of view. In contrast, only sporadic tumor nodules were observed in the lungs of the CTC NPs and CT NPs + laser groups, accompanied by a notable reduction in tumor infiltration. This indicated that both the targeted delivery of the drug on the nanoplatform and phototherapy were effective in inhibiting tumor metastasis. The lung tissue of the CTC NPs + laser group exhibited a significant reduction in metastatic foci, with a near-normal alveolar morphology and minimal tumor infiltration. This was attributed to the combination of high targeting efficiency and powerful photochemotherapy. In conclusion, these results suggest that the combination of CTC NPs and laser plays a significant role in inhibiting tumor growth and tumor metastasis by improving the biocompatibility and tumor targeting of CPT, which in turn combines with PDT/PTT.

The *in vivo* biosafety of the nanoplatform was further investigated. Hemolysis was negligible at high concentrations of CTC NPs (50 μmol/L) (Fig. S15 in Supporting information). The body weight of the mice in each group remained consistent throughout the course of treatment (Fig. S16 in Supporting information). This observation suggests that the nanoplatform developed in this study did not exhibit any notable systemic toxicity. Fresh blood was collected from each group at the end of treatment for hematological analysis (Fig. S17 in Supporting information) and blood biochemical analysis (Fig. S18 in Supporting information) to assess the effects of the materials on hematotoxicity and liver and kidney functions in mice. Malignant tumors have been reported to cause an increase in peripheral blood white blood cells (WBCs), suggesting entry into the terminal phase of the tumor [54]. After the different treatments, the WBCs counts of the mice in each group returned to normal levels to varying degrees. The WBCs counts in the CTC NPs + laser group were close to normal levels (Fig. S17), which accounted for only a small part of the inflammatory effect. There was no significant difference in any of the other hematological findings. This proved that CTC NPs had good biosafety and could reduce systemic inflammation.

All of the liver and kidney function indices indicated that CTC NPs were not systemically toxic, and the liver and kidney functions of the mice were not affected during treatment. The major organs of the mice were collected at the end of treatment to further assess the biosafety of CTC NPs. According to the organ indices (Fig. S19 in Supporting information), all organs except the spleen were morphologically normal. The spleens of all groups were enlarged to varying degrees by 4T1 tumors, and CTC NPs + laser had the least effect on spleen morphology, further demonstrating that CTC NPs combined with PDT/PTT reduced systemic inflammation. H&E staining of the major organs (heart, liver, spleen, and kidney) showed that the cellular morphology of the major organs was normal at the end of treatment in the different groups of mice, with no obvious pathological changes (Fig. S20 in Supporting information). In conclusion, CTC NPs can be used as a safe nanomedicine for *in vivo* tumor therapy.

This study leverages the multiple binding sites and hydrogen-bond stacking capabilities of CM-β-CD to construct self-assembled cyclodextrin-porphyrin nanoparticles (CT NPs). Designed for tumor-targeted delivery of the chemotherapeutic agent CPT, this nanoplatform enables multimodal synergistic therapy against breast cancer. Its unique photoresponsive mechanism concurrently mediates three antitumor responses under near-infrared (NIR) irradiation: (1) Localized hyperthermia *via* PTT, (2) efficient activation of the photosensitizer TAPP for PDT, and (3) spatiotemporally controlled CPT release. These components establish a self-reinforcing "PTT→PDT→Chemotherapy" cascade wherein photothermal acceleration of CPT release subsequently enhances phototherapeutic efficacy. The nanoplatform maintains CPT stability, circumvents RES clearance, and achieves tumor-specific accumulation, significantly enhancing intratumoral drug penetration and biocompatibility while preserving therapeutic potency. Critically, PDT-generated ROS acts synergistically with PTT-induced hyperthermia to promote tumor cell apoptosis, markedly amplifying CPT's antitumor efficacy. Concurrently, CTC NPs exploit intrinsic near-infrared fluorescence for precise tumor delineation and targeted imaging. In 4T1 subcutaneous tumor models, CTC NPs exhibited targeted delivery, favorable biosafety, and potent antitumor activity, effectively suppressing primary tumor progression (tumor suppression rate >95 %) and metastasis. Collectively, this cyclodextrin-porphyrin nanoplatform loaded with CPT demonstrates highly synergistic breast cancer treatment through integrated chemo-phototherapy mechanisms, while its inherent imaging functionality validates its translational promise as a tumor-targeted theranostic system.

Declaration of competing interest

The authors declare that they have no known competing financial interests or personal relationships that could have appeared to influence the work reported in this paper.

CRediT authorship contribution statement

Jiaojiao Yang: Writing – original draft, Project administration, Investigation, Data curation, Conceptualization. **Shaokun Yang:** Investigation, Data curation, Conceptualization. **Wei Cheng:** Investigation, Data curation, Conceptualization. **Jie Wu:** Investigation. **Haijing Qu:** Investigation. **Han Chen:** Investigation. **Zhiran Duan:** Investigation. **Yuqing Pan:** Investigation. **Ning Wang:** Investigation. **Chao Wang:** Investigation. **Jian Gao:** Investigation. **Bai Xiang:** Writing – review & editing, Funding acquisition, Data curation, Conceptualization. **Xiangdong Xue:** Writing – review & editing, Supervision, Data curation, Conceptualization.

Acknowledgments

This work was supported by the grants from the National Natural Science Foundation of China (No. 81973251), the Hebei Province Funding Project for Introduced Overseas Personnel (No. C20230351), and the Shijiazhuang Basic Research Project (No. 241791397A). 3d MAX and Biorender.com drew the Scheme.

Supplementary materials

Supplementary material associated with this article can be found, in the online version, at doi:10.1016/j.cclet.2025.111901.

References

[1] N. Harbeck, M. Gnant, Lancet 389 (2017) 1134–1150.
[2] M. Arnold, E. Morgan, H. Rumgay, et al., Breast 66 (2022) 15–23.

[3] J. Wang, Y. Fan, S. Xu, et al., Chin. Chem. Lett. 37 (2026) 111607.
[4] C. Yang, H. Liu, X. Feng, et al., Int. J. Surg. 110 (2024) 4976–4992.
[5] Y. Liang, H. Zhang, X. Song, Q. Yang, Semin. Cancer Biol. 60 (2020) 14–27.
[6] G. Curigliano, H.J. Burstein, E.P. Winer, et al., Ann. Oncol. 28 (2017) 1700–1712.
[7] S. Marsh, G. Liu, Adv. Drug Deliv. Rev. 61 (2009) 381–387.
[8] F. Poggio, M. Bruzzone, M. Ceppi, et al., J. Clin. Oncol. 36 (2018) 1497–1508.
[9] N. Khaiwa, N.R. Maarouf, M.H. Darwish, et al., Eur. J. Med. Chem. 223 (2021) 113639.
[10] A. Thomas, Y. Pommier, Clin. Cancer Res. 25 (2019) 6581–6589.
[11] M.D. Wang, D.Y. Hou, G.T. Lv, et al., Biomaterials 278 (2021) 121139.
[12] Y. Wang, Q. Tang, R. Wu, et al., ACS Nano 17 (2023) 3557–3573.
[13] M. Landgraf, C.A. Lahr, I. Kaur, et al., Biomaterials 240 (2020) 119791.
[14] M. Sun, H. Jiang, T. Liu, et al., Acta Pharm. Sin. B 12 (2022) 952–966.
[15] M. Su, Y. Chen, L. Jia, Z. Zhang, Int. J. Nanomed. 17 (2022) 6687–6705.
[16] D.J. Jang, C. Moon, E. Oh, Biomed. Pharmacother. 80 (2016) 162–172.
[17] M. Shahriari, S.M. Taghdisi, K. Abnous, M. Ramezani, M. Alibolandi, J. Control. Rel. 335 (2021) 369–388.
[18] R. Lagoa, J. Silva, J.R. Rodrigues, A. Bishayee, Biotechnol. Adv. 38 (2020) 107382.
[19] K. Yang, Z. Yang, G. Yu, et al., Adv. Mater. 34 (2022) e2107434.
[20] X. Dong, R.K. Brahma, C. Fang, S.Q. Yao, Chem. Sci. 13 (2022) 4239–4269.
[21] X. Xue, H. Qu, Y. Li, Exploration 2 (2022) 20210134.
[22] H. Li, M. Zhang, J. He, et al., Chin. Chem. Lett. 36 (2025) 110615.
[23] F. Tong, Y. Zhou, Y. Xu, et al., Exploration 3 (2023) 20210111.
[24] M.E. Davis, M.E. Brewster, Nat. Rev. Drug Discov. 3 (2004) 1023–1035.
[25] Y. Zhang, T. Sun, C. Jiang, Acta Pharm. Sin. B 8 (2018) 34–50.
[26] D. Sun, Y. Zou, L. Song, et al., Acta Pharm. Sin. B 12 (2022) 378–393.
[27] P. Lv, C. Zhou, Y. Zhao, X. Liao, B. Yang, Carbohydr. Polym. 168 (2017) 103–111.
[28] J. Li, X.J. Loh, Adv. Drug Deliv. Rev. 60 (2008) 1000–1017.
[29] S. Khammar, N. Bahramifar, H. Younesi, J. Hazard. Mater. 394 (2020) 122422.
[30] L. Chen, Y. Lin, Z. Zhang, et al., J. Nanobiotechn. 19 (2021) 329.
[31] P. Nonsuwan, P.P. Phiboonchaiyanan, N. Hirun, P. Kraisit, Carbohydr. Polym. 321 (2023) 121294.
[32] M. Zhou, Y. Long, Y. Zhi, X. Xu, Chin. Chem. Lett. 29 (2018) 1399–1403.
[33] A.G. Denkova, R.M. de Kruijff, P. Serra-Crespo, Adv. Healthc. Mater. 7 (2018) e1701211.
[34] X. Li, J.F. Lovell, J. Yoon, X. Chen, Nat. Rev. Clin. Oncol. 17 (2020) 657–674.
[35] W. Cheng, H.J. Qu, J.J. Yang, et al., ACS Nano 19 (2025) 557–579.
[36] W. Sun, X. Zhao, J. Fan, J. Du, X. Peng, Small 15 (2019) e1804927.
[37] L. Zhao, X. Zhang, X. Wang, et al., J. Nanobiotechn. 19 (2021) 335.
[38] H. Hu, W. Feng, X. Qian, et al., Adv. Mater. 33 (12) (2021) e2005062.
[39] W. Cheng, Z. Duan, H. Chen, et al., Acta Biomater. 193 (2025) 392–405.
[40] H. Chen, H. Qu, B. Lu, et al., Nanoscale 16 (2024) 14734–14747.
[41] H. Qu, L. Li, H. Chen, et al., J. Control. Rel. 363 (2023) 361–375.
[42] Z. Li, X. Wu, L. Li, et al., Chin. Chem. Lett. 37 (2026) 111501.
[43] S. Hu, W. Zhang, Z. Ni, et al., Chin. Chem. Lett. (2025), doi:10.1016/j.cclet.2025.111523.
[44] X. Xue, A. Lindstrom, Y. Li, Bioconjug Chem. 30 (2019) 1585–1603.
[45] M.S.H. Lim, T. Ohtsuki, F. Takenaka, et al., Life 11 (2021) 158.
[46] D. Wu, Z. Zhang, X. Li, et al., Acta Biomater. 168 (2023) 565–579.
[47] Y. Pan, H. Qu, H. Chen, et al., Acta Biomater. 193 (2025) 377–391.
[48] K. Yang, S. Qi, X. Yu, et al., Angew. Chem. Int. Ed. 61 (2022) e202203786.
[49] V.R. Pattabiraman, J.W. Bode, Nature 480 (2011) 471–479.
[50] M. Feng, H. Zhang, N. Maulide, Angew. Chem. Int. Ed. 134 (2022) e202212213.
[51] H. Bai, J. Wang, C.U. Phan, et al., Nat. Commun. 12 (2021) 759.
[52] L. Cao, H. Tian, M. Fang, et al., Biomaterials 290 (2022) 121856.
[53] X. Ge, Y. Hao, H. Li, et al., J. Nanobiotechn. 20 (2022) 369.
[54] A. Ocana, C. Nieto-Jimenez, A. Pandiella, A.J. Templeton, Mol. Cancer 16 (2017) 137.